Turbulence and Sheared Flow In Fusion Plasmas

Eduardo José Lascas Neto
edujln7@gmail.com

Instituto Superior Técnico, Lisboa, Portugal

September 2016

Abstract

The goal of this work consists in using a simple system of equations (derived in [1]) and extending to the nonlinear regime the linear results previously obtained.

To achieve this, a previously existent code was modified and the respective benchmark was done in the linear phase. Analytical tools for the study of the system in the nonlinear phase were found. The nonlinear numerical studies allowed to verify that the system in study contains zonal flows and that they are beneficial, since they reduce transport. An effect similar to the Dimits shift was observed. A reduction of transport by the action of an external shear flow was also observed, as well as turbulence caused by the PVG instability.

Keywords: Plasma Physics, Magnetic Confinement Fusion, Shear Flow, Plasma Turbulence, Turbulent Transport, Zonal Flows

1. Introduction

1.1. Motivation

It is well known that modern technology in advanced economies requires a huge consumption of energy, with electricity representing a major fraction of it [2]. The use of fossil fuels will likely change the environment as it increases the greenhouse effect and acidic pollution, which, by themselves contribute to global warming and the destruction of forests, respectively. As a consequence, it seems obvious that future energy production should not rely so heavily on fossil fuels.

In order to achieve fusion, one needs to confine the plasma composed by deuterium and tritium. Two primary methods can be used: magnetic confinement or inertial confinement. In this work we are interested in the magnetic confinement approach in which the plasma is confined via an imposed magnetic field. However, there are technical and scientific challenges to overcome, in order to have a good confinement of the plasma. One of the main problems to this confinement is the radial turbulent transport, which is the part of the total transport which arises form turbulence driven from micro-instabilities. Hence, a good understanding of these micro-instabilities and of the turbulence associated with them is crucial to increase the possibilities of having a sustainable fusion reaction.

1.2. State of the Art

In the vast majority of circumstances it is believed that anomalous transport is mostly due to an ion scale instability driven by the ion temperature gradient - the aptly baptized ion temperature gradient (ITG) instability [3]. There is also evidence that the turbulence created through this instability can be suppressed by an external shear flow ([4], [5], [6], [1]), generally created by neutral beam injection. However, another instability, called PVG (parallel velocity gradient), can also arise at high shear rates of the imposed shear flow (see [4], [5], [6], [1]).

Another well known physical phenomena are the zonal flows ([7], [8], [9]). Zonal flows are azimuthally symmetric band-like shear flows [8]. In fusion plasmas they can arise from self-generated and amplified $\boldsymbol{E} \times \boldsymbol{B}$ poloidal flows, which arise by electrostatic fluctuations generated by turbulent transport. Therefore, it is important to understand the competition between these three mechanisms: ITG, PVG, and shear flow. In this work we will try to study this phenomena using nonlinear numerical simulations. A simplified model of slab geometry and fluid equations [1] is used. The objective is that from the results of the simulations we can understand the simple physics of this model, which will in turn help to clarify some aspects of these effects in actual devices.

2. Theoretical Background

2.1. Theoretical Model Assumptions

The system considered [1] consists of an infinite plasma slab subjected to electrostatic perturbations in the presence of a sheared background magnetic field. The plasma is composed of two species,

namely, electrons and (hydrogenic) ions of mass m and charge e. Both species have an equal equilibrium density n_0. It is assumed that the electrons have an isothermal Boltzmann response [10] and therefore, the density perturbation δn_e of the electrons is given by

$$n_e = n_0 \exp\Big(\frac{e\phi}{T}\Big) \approx n_0\Big(1+\frac{e\phi}{T}\Big) \Rightarrow \delta n_e = n_0\frac{e\phi}{T}, \tag{1}$$

where T is the equilibrium temperature of both species and ϕ is the electrostatic potential. The ion response, however, is described by collisional fluid equations. These equations are derived from the gyrokinetic equation ([11]). The gyrokinetic approach assumes that the plasma is strongly magnetized and, therefore, a special ordering in the spatial and time scales can be used to reduce the total number of 6 coordinates of the Fokker-Planck equation. Namely, in gyrokinetics the following orderings are used:

$$\epsilon \sim \frac{\rho_i}{l_0} \sim \frac{\omega}{\Omega} \sim \mathcal{O}\Big(\frac{k_\parallel}{k_\perp}\Big) \sim \mathcal{O}\Big(\frac{\delta f}{F_0}\Big) << 1 \tag{2}$$

Here, ϵ is taken to be the expansion parameter, $\rho_i = v_{th}/\Omega$ is the ion gyro-radius, with $v_{th} = \sqrt{\frac{2T}{m}}$ the ion thermal velocity and Ω the cyclotronic frequency, $k_\parallel$ and $k_\perp$ are respectively the parallel and perpendicular wavelengths of the perturbation to the equilibrium, and l_o is the dimension of the system in the parallel direction (along the magnetic field lines). δf is the perturbed ion distribution function and F_0 is the equilibrium Maxwellian. This is the ordering of the primary expansion which is done on the gyrokinetic equation [1].

A second expansion is also performed, which is motivated by the collisional limit that we wish to consider. The orderings considered are the following

$$\nu_i >> \omega, \omega^*, v_{th}k_\parallel, u_f k_\parallel, \nu_i k^2\rho_i^2, \tag{3}$$

where ν_i is the ion-ion collision frequency, ω^* is the typical frequency of the drift waves associated with the background gradients of the system. Throughout these expansions the form of the Maxwellian of equilibrium is defined by the background gradients of the equilibrium density, the equilibrium temperature and the shear flow. A transformation of coordinates that accounts the geometry of the background magnetic field and shear flow is also performed, in order to clarify the effect of the shear flow.

2.2. Geometry

The system we wish to consider consists of an infinite plasma slab in the presence of a background sheared magnetic field and shear flow, which are given respectively by

$$\boldsymbol{B} = B_0\Big(\hat{e_z} + \frac{x}{l_s}\hat{e_y}\Big), \tag{4}$$

$$\boldsymbol{V_0} = V_0\frac{x}{L_v}\hat{e_v} = V_0\frac{x}{L_v}(\hat{e_v}\cdot\hat{e_y})\hat{e_y} + V_0\frac{x}{L_v}(\hat{e_v}\cdot\hat{e_z})\hat{e_z}, \tag{5}$$

where $\hat{e_v}$ is a unit vector in the (y,z)-plane, and l_s and L_v are, respectively, the characteristic scale lengths of the magnetic field and flow variation in the x-direction. These fields can be seen as linear approximations of the Taylor series expansions in the parameters $x/l_s \ll 1$ and $x/L_v \ll 1$ of the general forms of the background magnetic field and shear flow, respectively.

The sheared background magnetic field appears in order to model the magnetic field that is present on a tokamak. Roughly speaking we could say that the toroidal component would correspond in this slab case to the direction defined by the unit vector $\hat{e_v}$, while the poloidal and radial components would correspond to the y and x components, respectively. Thus, the background magnetic field of equation (4), tries to simulate the real magnetic field used on tokamaks, which is composed of a toroidal component and a weaker poloidal component with a shear in the radial direction. The background shear flow is chosen to emulate the external shear flow imposed on tokamaks in order to reduce transport. These flows are, usually, toroidal flows. Therefore, they have one component perpendicular to the magnetic field and another one parallel to the magnetic field. The background flow in this system is chosen in order to retain these characteristics, as one can see in equation (5) because those components have in general different effects on the plasma as already stated. The perpendicular component is stabilizing while the parallel one can be destabilizing via the PVG instability. The effect of the background magnetic field in perturbations is shown in figure 1, while figure 2 shows the effect of the background shear flow in perturbations. In this work, two sets of transformations are combined. One accounts for the effect of the shear of the magnetic field and the another one accounts for the effect of the shear flow, in oder to clarify the effects of the component of the shear flow perpendicular to the magnetic field lines and the component of the shear flow parallel to the magnetic field lines. The first will appear as a convective velocity u_f in the new z-direction, while the second will appear as a drive term of the PVG instability. Combining the two sets of transformations, we obtain the final set of coordinates given by

$$t' = t, \qquad x' = x, \qquad y' = y - \frac{x}{l_s}z', \qquad z' = z + u_f t, \tag{6}$$

where

$$u_f = V_0\frac{l_s}{L_v}(\hat{e_V}\cdot\hat{e_y}) \tag{7}$$

is the velocity of convection of the eddies. Transformation (6) will be used to study this system and is called "twisted-sheared representation" [12].

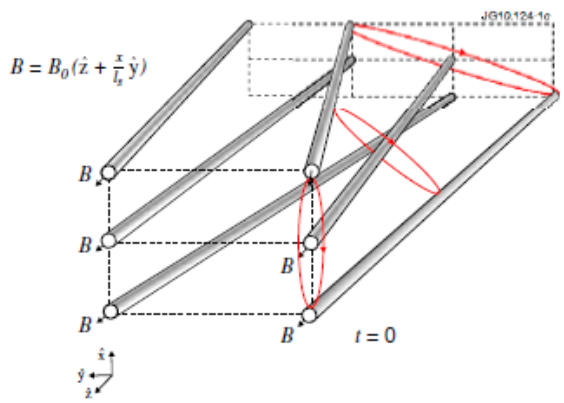

Figure 1: Effect of the background sheared magnetic field on the magnetic field lines, represented by flux tubes, and on the eddies, whose cross-section along the z-direction is represented by the red ovals. Note that this happens at $t = 0$. The eddies will twist with the shear of the magnetic field, in order to remain in surfaces where the plasma retains its natural response. Hence, the cross-section of the eddies suffers a tilt as it follows the magnetic field lines. Reproduced from [1].

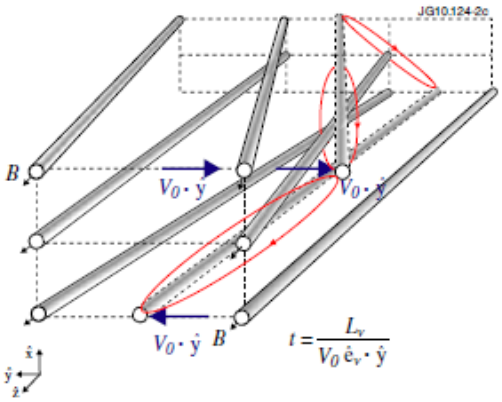

Figure 2: Effects of the background perpendicular sheared flow on the magnetic field lines and on the eddies. Note that this happens at $t = t_s = l_s/u_f$, with t_s the characteristic time. The effect of the perpendicular component of the sheared flow can be seen as a convection of the eddies in the negative z-direction at a velocity $-u_f$. During a characteristic time t_s the cross-section of the eddy which was vertical in $x = 0$, at a time $t = 0$ moved to $z = -l_s$, where l_s is the characteristic length associated with the shear of the magnetic field. Reproduced from [1].

2.3. System Equations

Using the expansions referred and the "twisted-sheared representation" (see [1]). the fluid equations of the system for the perturbed normalized ion density n, ion parallel velocity V and ion temperature T can be written as

$$\Big(\frac{\partial}{\partial t} + M\frac{\partial}{\partial z}\Big)n + \frac{\partial V}{\partial z} = \frac{3}{8}\frac{l_s}{l_n}\frac{\partial n}{\partial y}, \tag{8}$$

$$\Big(\frac{\partial}{\partial t} + M\frac{\partial}{\partial z}\Big)V + \frac{3}{8}\frac{\partial}{\partial z}(2n+T) + \frac{3}{8}\{n, V\} = \frac{3}{8}\frac{l_s}{l_V}\frac{\partial n}{\partial y} + \nu_\perp \nabla_\perp^2 V, \tag{9}$$

$$\Big(\frac{\partial}{\partial t} + M\frac{\partial}{\partial z}\Big)T + \frac{2}{3}\frac{\partial V}{\partial z} + \frac{3}{8}\{n, T\} = \frac{3}{8}\frac{l_s}{l_T}\frac{\partial n}{\partial y} + \chi_\perp \nabla_\perp^2 T \tag{10}$$

where the following normalizations were used

$$x' = \rho_s \tilde{x}, \qquad y' = \rho_s \tilde{y}, \qquad z' = l_s \tilde{z}, \qquad t' = \frac{l_s}{c_s}\tilde{t} \tag{11}$$

$$\tilde{V} = \frac{\delta V_\parallel}{c_s}\frac{l_s}{\rho_s}, \qquad \tilde{T} = \frac{\delta T}{T}\frac{l_s}{\rho_s}, \qquad \tilde{n} = \frac{\delta n}{n_0}\frac{l_s}{\rho_s} \tag{12}$$

and the tildes denoting the final transformation were dropped. The sound Larmor radius is defined as $\rho_s = c_s/\Omega$ and $c_s = \sqrt{\frac{(\gamma_e+\gamma_i)T}{m}}$ it's the sound speed, in which, $\gamma_e = 1$ (electron Boltzmann response) and $\gamma_i = 5/3$ (ion adiabatic response). The diffusion operator is given by

$$\nabla_\perp^2 = \frac{\partial^2}{\partial y^2} + \Big(\frac{\partial}{\partial x} - z\frac{\partial}{\partial y}\Big)^2 \tag{13}$$

and the Poisson parenthesis can be written as

$$\{p, h\} = (\nabla p \times \nabla q)\cdot \hat{b} = \frac{\partial p}{\partial x}\frac{\partial q}{\partial y} - \frac{\partial p}{\partial y}\frac{\partial q}{\partial x}. \tag{14}$$

where $\hat{b} = \boldsymbol{B}/B$. The ion response is driven by the background gradients which are defined by the characteristic lengths

$$\frac{1}{l_n} = \frac{d}{dx}\ln(n_0(x)), \qquad \frac{1}{l_T} = \frac{d}{dx}\ln(T(x)), \qquad \frac{1}{l_V} = \frac{1}{L_v}\frac{V_0}{c_s}(\hat{e_V}\cdot\hat{e_z}). \tag{15}$$

An effective Mach number M related with the convective effect of the perpendicular shear flow is also introduced and is defined as

$$M = \frac{u_f}{c_s}. \tag{16}$$

The normalized diffusion coefficients are defined as

$$(\nu_\perp, \chi_\perp) = \frac{1}{c_s\rho_s^2/l_s}(\nu, \chi) = \Big(\frac{9}{40}, \frac{1}{4}\Big)\sqrt{\frac{2}{3}}\frac{l_s n_0 e^4 \ln\Lambda}{8\pi^{3/2}\varepsilon_0^2 T^2}, \tag{17}$$

where the definition of the ion collision ν_i has been used:

$$\nu_i = \frac{e^4\ln\Lambda}{8\pi\varepsilon_0^2 m^2}, \tag{18}$$

in which Λ is the Coulomb logarithm.

2.4. Instabilities with $M = 0$

In the case of no perpendicular component of the external flow ($M = 0$) a linear analysis of the effect of the dissipations on the perturbations can be done [1]. Choosing $\chi_\perp = 0$ which corresponds to a system with an artificially large Prandtl number $P_t = \nu_\perp/\chi_\perp \gg 1$ and neglecting the nonlinear terms one can find an instability with a linear growth rate γ given by

$$\frac{a}{b}(\gamma + \nu_k) + (2n+1)\sqrt{\frac{a\nu_k}{b}} - \frac{\omega_v^{*^2}}{4b^2} = 0, \qquad (19)$$

where $a = \gamma - i\omega_n^*$, $b = 1 + \frac{i}{4\gamma}(-\omega_n^* + \frac{3}{2}\omega_T^*)$ and $\nu_k = \nu_\perp k_y^2$. ω_n^*, ω_T^* and ω_V^* are the frequencies related with the drift waves, which will generate the universal ([13]), the ITG ([14]) and the PVG ([15]) instabilities. These frequencies are defined as:

$$\omega_n^* = k_y \frac{3}{8}\frac{l_s}{l_n}, \qquad \omega_V^* = k_y \frac{3}{8}\frac{l_s}{l_V}, \qquad \omega_n^* = k_y \frac{3}{8}\frac{l_s}{l_T}. \qquad (20)$$

Equation (19) can be solved with the help of a numerical package software such as *Mathematica*. The solution of this equation for the parameters $l_s/l_n = 3$, $l_s/l_V = 9$ $l_s/l_T = 6$ and $\nu_\perp = 3$ can be seen in figure 3, in section 3, where a benchmarking against the numerical solutions of the code is done.

2.5. Characteristics Form of the System

The system of equations can be written in characteristics form. This result is important to the application of the numerical method used. To cast the system in characteristics form the following new quantities have to be defined

$$S = \frac{3}{2}T - n, \qquad C^+ = V + \frac{3}{4}\Big(n + \frac{T}{2}\Big), \qquad C^- = V + \frac{3}{4}\Big(n + \frac{T}{2}\Big). \qquad (21)$$

which are the entropy wave S, and two sound waves C^+ and C^-. C^+ is a sound wave which propagates at speed $M+1$, while C^- is a wave that propagates at speed $M-1$. The drift wave associated with each of these quantities have the following frequencies:

$$\omega_S^* = \frac{3}{2}\omega_T^* - \omega_n^*, \qquad \omega_+^* = \omega_V^* + \frac{3}{4}\Big(\omega_n^* + \frac{\omega_T^*}{2}\Big), \qquad \omega_-^* = \omega_V^* - \frac{3}{4}\Big(\omega_n^* + \frac{\omega_T^*}{2}\Big). \qquad (22)$$

2.6. Zonal Flows

In order to investigate the presence of zonal flows in the system, equations for the zonal components of the perturbations can be found. In general the zonal $\langle f\rangle$ and non-zonal $\tilde{f}$ components of a perturbation f can be defined, respectively, as (see [16]):

$$\langle f\rangle = \frac{1}{L_y}\int f dy, \qquad \tilde{f} = f - \langle f\rangle. \qquad (23)$$

where L_y is the size of the box in the y-direction. Therefore, the system equations for zonal components can be obtained by averaging the equations (8)-(10) in the y-direction. Doing this we obtain:

$$\Big(\frac{\partial}{\partial t} + M\frac{\partial}{\partial z}\Big)\langle n\rangle + \frac{\partial\langle V\rangle}{\partial z} = 0, \qquad (24)$$

$$\Big(\frac{\partial}{\partial t} + M\frac{\partial}{\partial z}\Big)\langle V\rangle + \frac{3}{8}\frac{\partial}{\partial z}(2\langle n\rangle + \langle T\rangle) = -\frac{3}{8}\frac{\partial}{\partial x}\langle V\tilde{V}_x\rangle + \nu_\perp\frac{\partial^2\langle V\rangle}{\partial x^2}, \qquad (25)$$

$$\Big(\frac{\partial}{\partial t} + M\frac{\partial}{\partial z}\Big)\langle T\rangle + \frac{2}{3}\frac{\partial\langle V\rangle}{\partial z} = -\frac{3}{8}\frac{\partial}{\partial x}\langle T\tilde{V}_x\rangle + \chi_\perp\frac{\partial^2\langle T\rangle}{\partial x^2}, \qquad (26)$$

in which $\tilde{V}_x = \frac{\partial\tilde{n}}{\partial y}$. According to these equations the presence of zonal flows is expected and they are generated by a term similar to the Reynolds stress.

2.7. System Invariant

One invariant of the system of equations (8)-(10) can be obtained by multiplying each equation by the respective quantity and then integrate the equations in a box of length L_x, L_y and $L_z \to \infty$. Then we obtain the conservation equation:

$$\frac{dW}{dt} = \Gamma - D \qquad (27)$$

where

$$W = \iiint \Big(\frac{3}{8}|n|^2 + \frac{1}{2}|V|^2 + \frac{9}{32}|T|^2\Big)dxdydz \qquad (28)$$

is the invariant of the system of equations. The flux Γ is given by the integration of the drive terms

$$\Gamma = \Gamma_n + \Gamma_V + \Gamma_T = \iiint \Big(\frac{9}{32}\frac{l_s}{l_n}\frac{\partial\tilde{n}}{\partial y}\tilde{n} + \frac{3}{8}\frac{l_s}{l_V}\frac{\partial\tilde{n}}{\partial y}\tilde{V} + \frac{27}{128}\frac{l_s}{l_T}\frac{\partial\tilde{n}}{\partial y}\tilde{T}\Big)dxdydz \qquad (29)$$

and the diffusion D is given by the integration of the dissipations in the perpendicular direction

$$D = D_v + D_T = \iiint \Big(\nu_\perp\nabla_\perp^2 VV + \frac{9}{16}\chi_\perp\nabla_\perp^2 TT\Big)dxdydz \qquad (30)$$

This invariant is important as it is proportional to the value of the transport in the system. Therefore, from the behavior of this invariant in the turbulent phase of the system, one can take conclusions about the turbulent transport in the system. It can also be shown that the zonal and non-zonal components of the invariants constitute themselves a predator-prey system where the preys are the non-zonal components and the predators are the zonal components. In a system with this behavior Dimits shift-like effects ([17]) are expected.

2.8. Stability of zonal flows

We can analyze the presence of the Dimits shift in this system linearly with the analysis of the stability of the zonal flows generated in the nonlinear phase. We start by considering an equilibrium state composed of pure zonal flows $u_0(x)$, which can suffer perturbations of the type $\tilde{u} = \tilde{u}(x)\exp(\gamma t + ik_y y + ik_\parallel z)$, where γ corresponds to the linear growth rate of potential zonal flow instabilities. Considering these equilibrium and perturbation for the quantities n, V and T , this possible linear growth rate is given by

$$\gamma_n^2(\gamma' - i\omega_n^*) + \frac{1}{4}k_\parallel^2(\gamma' - i\omega_n^*) - k_\parallel\Big(k_y\frac{3}{8}V'_0(x) + \omega_V^* - \frac{3}{4}k_\parallel\Big)\gamma_n + i\frac{3}{8}k_\parallel^2\Big(k_y\frac{3}{8}T'_0(x) + \omega_T^*\Big) = 0, \tag{31}$$

where $\gamma' = \gamma + ik_\parallel M$ and $\gamma_n = \gamma' + ik_y\frac{3}{8}n'_0(x)$. If no linear growth is found, then the zonal flows are stable and can effectively reduced transport.

3. Numerical Code Implementation

In this work, the numerical code *Viriato* is used ([18]). *Viriato* is a 3D code and pseudo-spectral code, as it is spectral in the xy-plane and grid-based in the z-direction. The code is parallelized with MPI in the z and y-directions in real space and in the x and y-directions in Fourier space. This code was modified so it could solve equations (8)-(10). The equations solved by *Viriato* can be solved numerically using a Godunov splitting ([18]) of the terms with spatial derivatives. Thus, the computational cycle which consists of one time cycle is divided in two parts. First, it advances the timestep accounting only terms affected by operators acting in the perpendicular direction. Second, it advances the timestep accounting only terms affected by operators acting in the parallel direction. Equations (8)-(10) have some similarities in their form to equations solved in *Viriato* (see [18]). Hence, in this work we use this fact and adapt the code of *Viriato*, in order to be able to solve equations (8)-(10). Thus, time stepping algorithm can be divided in two main steps, resulting from the Godunov split, the perpendicular step and the parallel step.

3.1. Perpendicular Step

The code starts with the perpendicular step. In this part, all the quantities are advanced in time taking into account the terms with operators acting in the perpendicular directions x and y. Thus, the equations to be solved numerically in this step are given by

$$\frac{\partial n}{\partial t} = \hat{\rho_s}\frac{3}{8}\frac{l_s}{l_n}\frac{\partial n}{\partial \hat{y}}, \tag{32}$$

$$\frac{\partial V}{\partial t} = \hat{\rho_s}\frac{3}{8}\frac{l_s}{l_V}\frac{\partial n}{\partial \hat{y}} - \hat{\rho_s}^2\frac{3}{8}\{n, V\} + \hat{\rho_s}^2\nu_\perp\nabla_\perp^2 V, \tag{33}$$

$$\frac{\partial T}{\partial t} = \hat{\rho_s}\frac{3}{8}\frac{l_s}{l_T}\frac{\partial n}{\partial \hat{y}} - \hat{\rho_s}^2\frac{3}{8}\{n, T\} + \hat{\rho_s}^2\chi_\perp\nabla_\perp^2 T. \tag{34}$$

Here, $\hat{\rho_s} = \rho_s/L_\perp$ which is the sound Larmor radius normalized according to *Viriato* normalizations which are given by

$$\hat{x} = x'/L_\perp, \quad \hat{y} = y'/L_\perp, \quad \hat{z} = z'/L_\parallel. \tag{35}$$

The notation $\hat{X}$ means that the quantity X is normalized according equation (35). The code solve these equations in the Fourier space as in the original code of *Viriato*. So applying a Fourier transform $\mathcal{F}$ the previous equations take the form

$$\frac{\partial n_k}{\partial t} = i\hat{\rho_s}\frac{3}{8}\frac{l_s}{l_n}\hat{k_y}n_k, \tag{36}$$

$$\frac{\partial V_k}{\partial t} = i\hat{\rho_s}\frac{3}{8}\frac{l_s}{l_V}\hat{k_y}V_k - \hat{\rho_s}^2\frac{3}{8}\mathcal{F}\Big(\{n, V\}\Big) - \mathcal{D}_\nu V_k, \tag{37}$$

$$\frac{\partial T_k}{\partial t} = i\hat{\rho_s}\frac{3}{8}\frac{l_s}{l_T}\hat{k_y}V_k - \hat{\rho_s}^2\frac{3}{8}\mathcal{F}\Big(\{n, T\}\Big) - \mathcal{D}_\chi T_k, \tag{38}$$

where

$$\begin{aligned}\mathcal{D}_\nu &= \hat{\rho_s}^2\nu_\perp(k_x^2 - 2zk_xk_y + (1+z^2)k_y^2),\\ \mathcal{D}_\chi &= \hat{\rho_s}^2\chi_\perp(k_x^2 - 2zk_xk_y + (1+z^2)k_y^2),\end{aligned} \tag{39}$$

and for a quantity X we have

$$X_k = \mathcal{F}(X). \tag{40}$$

Equations (36)-(38) are similar to those solved in [19]. Thus, they are solved using the same numerical method used in [19], which is a semi-implicit numerical method that treats the dissipative terms in an implicit way. The predictor step is then given by

$$n^*{}_k = n_k^t + \Delta t\Big(i\hat{\rho_s}\frac{3}{8}\frac{l_s}{l_n}\hat{k_y}n_k^t\Big), \tag{41}$$

$$V^*{}_k = e^{-\mathcal{D}_\nu\Delta t}V_k^t + \frac{\Delta t}{2}\Big(1 + e^{-\mathcal{D}_\nu\Delta t}\Big)\Big(i\hat{\rho_s}\frac{3}{8}\frac{l_s}{l_V}\hat{k_y}n_k^t - \hat{\rho_s}^2\frac{3}{8}\mathcal{F}\Big(\{n^t, V^t\}\Big)\Big), \tag{42}$$

$$T_k^* = e^{-\mathcal{D}_\chi\Delta t}T_k^t + \frac{\Delta t}{2}\Big(1 + e^{-\mathcal{D}_\chi\Delta t}\Big)\Big(i\hat{\rho_s}\frac{3}{8}\frac{l_s}{l_T}\hat{k_y}n_k^t - \hat{\rho_s}^2\frac{3}{8}\mathcal{F}\Big(\{n^t, T^t\}\Big)\Big). \tag{43}$$

The corrector step gives the quantities at a time $t+1$ for the perpendicular step and can be written as

$$V_k^{t+1} = e^{-\mathcal{D}_\nu\Delta t}V_k^t + \frac{\Delta t}{2}e^{-\mathcal{D}_\nu\Delta t}\Big(i\hat{\rho_s}\frac{3}{8}\frac{l_s}{l_V}\hat{k_y}n_k^t - \hat{\rho_s}^2\frac{3}{8}\mathcal{F}\Big(\{n^t, V^t\}\Big)\Big) + \frac{\Delta t}{2}e^{-\mathcal{D}_\nu\Delta t}\Big(i\hat{\rho_s}\frac{3}{8}\frac{l_s}{l_V}\hat{k_y}n_k^* - \hat{\rho_s}^2\frac{3}{8}\mathcal{F}\Big(\{n^*, V^*\}\Big)\Big), \tag{44}$$

$$n_k^{t+1} = n_k^t + \frac{\Delta t}{2}\Big(i\hat{\rho_s}\frac{3}{8}\frac{l_s}{l_n}\hat{k_y}n_k^t + i\hat{\rho_s}\frac{3}{8}\frac{l_s}{l_n}\hat{k_y}n_k^*\Big), \tag{45}$$

$$T_k^{t+1} = e^{-\mathcal{D}_\chi \Delta t} T_k^t + \frac{\Delta t}{2} e^{-\mathcal{D}_\chi \Delta t}\Big(i\hat{\rho_s}\frac{3}{8}\frac{l_s}{l_T}\hat{k_y} n_k^t - \hat{\rho_s}^2 \frac{3}{8}\mathcal{F}\Big(\{n^t, T^t\}\Big)\Big) + \frac{\Delta t}{2} e^{-\mathcal{D}_\chi \Delta t}\Big(i\hat{\rho_s}\frac{3}{8}\frac{l_s}{l_T}\hat{k_y} n_k^{t+1} - \hat{\rho_s}^2 \frac{3}{8}\mathcal{F}\Big(\{n^{t+1}, T^*\}\Big)\Big). \quad (46)$$

In these two steps the Fourier transforms of the Poisson brackets are calculated in the following way (as in *Viriato*). First, the quantities X_k in the Fourier space are obtained, then one multiplies these quantities by ik_x or ik_y and an inverse Fourier transform is performed to obtain $\mathcal{F}^{-1}(ik_x X_k) = \partial X/\partial x$. When all the needed terms of this type are obtained the Poisson bracket operations are performed in the real space and, finally, the Fourier transform of the Poisson bracket is calculated in order to obtain the needed terms in the previous equations. This is the reason the method is called pseudo-spectral, instead of just spectral

3.2. Parallel Step

The parallel step solves the remaining part of the equations. In this step all quantities are advanced taking into account the remaining terms, which are the terms affected by derivatives in the parallel or z-direction. Thus, the equations to be solved numerically in this step can be written in the characteristic form and in the Fourier space as

$$\frac{\partial S_k}{\partial t} = -M\frac{\partial S_k}{\partial z}, \quad (47)$$

$$\frac{\partial C_k^+}{\partial t} = -(M+1)\frac{\partial C_k^+}{\partial z}, \quad (48)$$

$$\frac{\partial C_k^-}{\partial t} = -(M-1)\frac{\partial C_k^-}{\partial z}. \quad (49)$$

In the beginning of the parallel step, the quantities S_k, C_k^+ and C_k^- are obtained from the quantities n_k, V_k and T_k obtained in the perpendicular step. Then the parallel step is done using the second order upwind scheme (see, e.g ., [20]), which is given by

$${S_k}_p^{t+1} = {S_k}_p^t - \frac{M\Delta t}{2\Delta z}\Big(3{S_k}_p^t - 4{S_k}_{p-1}^t + {S_k}_{p-2}^t\Big), \quad (50)$$

$${C_k^+}_p^{t+1} = {C_k^+}_p^t - \frac{(M+1)\Delta t}{2\Delta z}\Big(3{C_k^+}_p^t - 4{C_k^+}_{p-1}^t + {C_k^+}_{p-2}^t\Big), \quad (51)$$

$$\begin{cases} {C_k^-}_p^{t+1} = {C_k^-}_p^t - \frac{(M-1)\Delta t}{2\Delta z}\Big(3{C_k^-}_p^t - 4{C_k^-}_{p-1}^t + {C_k^-}_{p-2}^t\Big), \\ \quad if \quad M-1 \geq 0 \\ {C_k^-}_p^{t+1} = {C_k^-}_p^t + \frac{(M-1)\Delta t}{2\Delta z}\Big(3{C_k^-}_p^t - 4{C_k^-}_{p-1}^t + {C_k^-}_{p-2}^t\Big), \\ \quad if \quad M-1 < 0, \end{cases} \quad (52)$$

where p is the index of the discretization in the z direction. The open boundary conditions are also applied. Because *Viriato* is parallelized in the z-direction, the implementation of this scheme requires communication between processors to obtain the boundary values.

3.3. CFL Conditions

The last essential part of the computational cycle used in this work is the application of the CFL condition (see, e. g, [21]) at the end of each time cycle in order to achieve numerical stability. In this system the CFL condition is given by

$$\Delta t = \alpha_{CFL} \cdot min\Big[\frac{dz}{M+1}, \frac{1}{\hat{\rho_s}}\frac{2}{max(\omega_S^*)}, \frac{1}{\hat{\rho_s}}\frac{2}{max(\omega_+^*)}, \frac{1}{\hat{\rho_s}}\frac{2}{max(\omega_-^*)}, \frac{1}{\hat{\rho_s}^2}\frac{8}{3max(k_x k_y n)}\Big], \quad (53)$$

where $\alpha_{CFL} < 1$. This ends the computational cycle of the code used in this work.

3.4. Benchmark

In this section we present the results obtained to benchmark the adapted code. As it was said in section 2.4, the benchmark is done against an analytical solution of equation (19). Therefore, to achieve the results needed for benchmarking, numerical runs were made for the following input parameters: $M = 0$, $l_s/l_n = 3$, $l_s/l_V = 9$, $l_s/l_T = 6$, $\nu_\perp = 3$ and $\chi_\perp = 0$. A total of 10 runs were made with these parameters fixed, while changing the value of k_y of the initial perturbation. An initial perturbation n is given in the Fourier space, in order to select only the desired mode in the y-direction. This perturbation can be written as

$$\begin{cases} n_k(t=0, k_x, k_y, z) = e^{-\frac{z^2}{6}}, \quad if \quad |k_y| = \frac{2\pi}{L_y} \\ n_k(t=0, k_x, k_y, z) = 0, \quad otherwise \end{cases}. \quad (54)$$

Using this perturbation, the runs were made for different values of k_y between $k_y = 0.1$ and $k_y = 1.0$ with intervals between the values of k_y of 0.1. Fits were done to the timetraces in order to obtain the linear growth γ and the oscillatory frequency ω for all ten values of k_y. The results of the benchmarking are presented in figures 3 and 4. The value of k_y is choose by changing the value of L_y. The other box parameters are fixed at $L_x = 2\pi\rho_s$ and $Lz = 200\pi$. In terms of resolution the parameters used are $nlx = 8$, $nly = 16$ and $nlz = 1024$. Where nlz was chosen to guarantee convergence for all values of k_y used.

4. Numerical Results

In this chapter the numerical nonlinear results are presented. In these results the initial perturbation is given in the real space and has a Gaussian form, which in normalized form, can be written as

$$n(t=0, x, y, z) = e^{-\frac{x^2}{6}} e^{-\frac{y^2}{6}} e^{-\frac{z^2}{6}}. \quad (55)$$

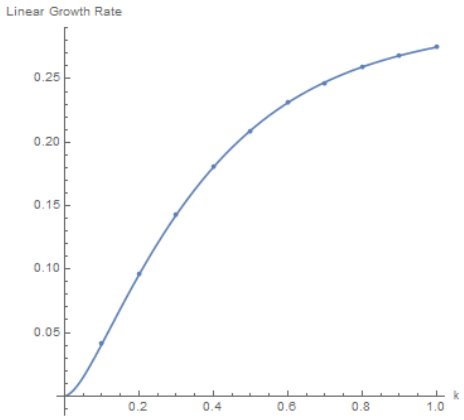

Figure 3: Benchmark of the adapted code against the linear growth rate of the analytical solution of (19) for the input parameters $M = 0$, $l_s/l_n = 3$, $l_s/l_V = 9$, $l_s/l_T = 6$, $\nu_\perp = 3$ and $\chi_\perp = 0$.

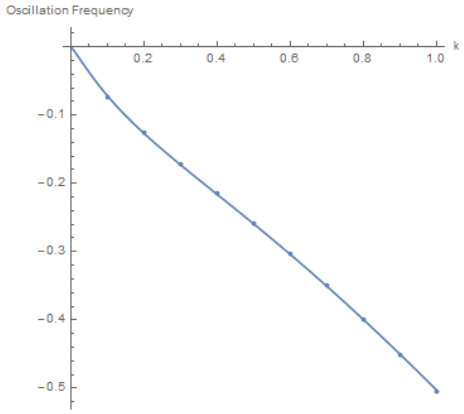

Figure 4: Benchmark of the adapted code against the oscillation frequency of the analytical solution of (19) for the input parameters $M = 0$, $l_s/l_n = 3$, $l_s/l_V = 9$, $l_s/l_T = 6$, $\nu_\perp = 3$ and $\chi_\perp = 0$.

This perturbation is used, so that in all directions the most unstable mode is captured, of all the modes allowed by the resolution parameters used. The input parameters and resolution parameters will change, depending on the cases of study. The dissipations coefficients are kept at relatively large values $\nu_\perp = 3$ and $\chi_\perp = 10/3$ to ensure the consistency of our orderings, as in [1].

4.1. Nonlinear finite l_s/l_T

Here, nonlinear results with only finite l_s/l_T are presented. Using the initial perturbation given in equation (55) nonlinear runs were made for different values of l_s/l_T, keeping $l_s/l_n = 0$, $l_s/l_V = 0$ and $M = 0$, so that the effects of pure ITG turbulence could be studied. In this limit the presence of zonal flows in the system is investigated as the external flow is set to 0. Runs were made for values of the temperature gradient from $l_s/l_T = 28$ to $l_s/l_T = 40$ in order to be near the critical value of l_s/l_T for linear instability. In this case this value is found to be $l_s/l_T = 28$, as for this value of l_s/l_T no instability is numerically observed. This value differs from the values found in [1] because the resolution parameters used in these runs are different. For this case we used $nlx = 64$ and $nly = 64$ and a box of perpendicular lengths of $L_x = L_y = 2\pi = 32\rho_s$. Therefore, perpendicular modes that can be captured are given by $k_x = k_y = n/(32\rho_s)$ with $n = 0, ..., 32$. This resolution in the xy-plane was chosen due to numerical constraints in terms of computational time. In the parallel direction a box of size $L_z = 50\pi$ is used, with a resolution parameter of $nlz = 256$. Thus, the resolution in the parallel direction is smaller than the resolution used in [1] of $\Delta z = 0.1$. Hence, the critical value of l_s/l_T captured is bigger than in [1], as the growth rate values captured become smaller with a decreasing resolution in Δz. The theoretical value of this critical value of l_s/l_T can not be obtained analytically for both finite values of $\nu_\perp$ and $\chi_\perp$, but in the numerical linear analysis done in [1] it was found that for $\Delta z = 0.1$, it should lie between $l_s/l_T = 20$ and $l_s/l_T = 25$. The choose of this reduced value of resolution in z with respect to [1] has to due with numerical constraints in terms of computational time. However, the nonlinear effects captured should be similar as one expects that the change of growth rate only changes the instant in which the nonlinear phase starts.

The timetraces of the invariant for the different values of l_s/l_T can be obtained and are presented in 5. Here we use the total invariant W as a measure of the turbulent transport, because one cannot retrieve the turbulent coefficients as in usual gyrokinetic simulations. Runs were also made for $l_s/l_T/ = 25$ and $l_s/l_T = 28$. However, as it was not observed any linear instability (and therefore no turbulent transport) for these runs, they are not shown in figure 5. As was referred in section 2.6, this simple system should be able to capture simple aspects of the zonal flows in the form of zonal components which are generated by a similar mechanism to the Reynolds stress. In the case of finite l_s/l_T the presence of zonal flows can be observed, for example in figure 6, in which the timetrace of the zonal component of the invariant is showed against the total invariant. We can see that the zonal component of the invariant $\langle W \rangle$ grows to a finite value, which indicates the presence of zonal components in the system. Moreover we can see that when the zonal component of the invariant grows there is a correspondent decrease in the value of the total invariant. This shows the characteristic predator-prey behavior between the zonal components and the drift waves in the system, as was predicted in section 2.7.

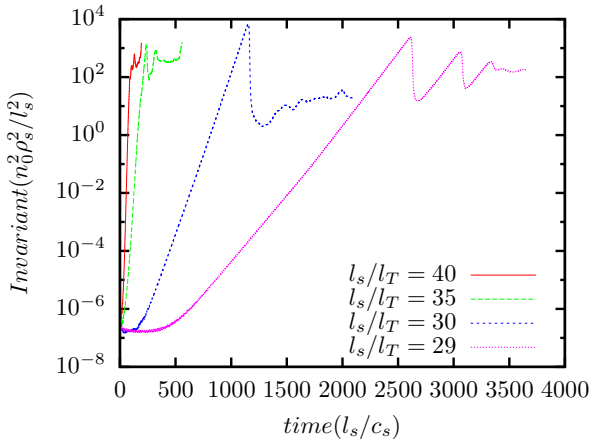

Figure 5: Timetraces of the total invariant for different values of l_s/l_T. The other input parameters are fixed at $l_s/l_n = 0$, $l_s/l_V = 0$, $M = 0$.

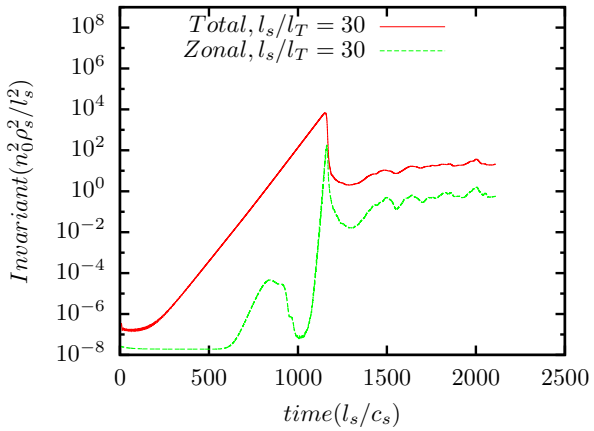

Figure 6: Timetraces of the total invariant and the zonal invariant for $l_s/l_T = 30$. The other input parameters are fixed at $l_s/l_n = 0$, $l_s/l_V = 0$, $M = 0$.

Then, a similar effect to a Dimits shift should be observed. The Dimits shift [17] is an effect which was first observed for a collisionless plasma. In a collisionless plasma the primary dissipation mechanism of the zonal flows is absent. Thus, they can increase seamlessly and for values of temperature gradient near the critical value for linear instability they cause a total quench of ITG turbulent transport. In this case the mean value of the total invariant in the turbulent phase should be directly proportional to the turbulent transport. In figure 7 we obtain these values for the previous runs, in order to clarify the reduction of turbulent transport near the linear critical value of l_s/l_T. The null values of turbulent transport for the runs with $l_s/l_T = 25$ and $l_s/l_T = 28$ are also included and correspond to the cases where no linear instability is observed. We see that there is a considerable uncertainty for the cases $l_s/l_T = 35$ and $l_s/l_T = 40$. This is due to the fact that these runs have not run for long enough to reach a statistical steady-state.

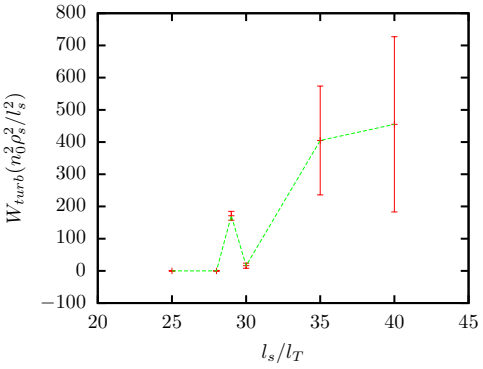

Figure 7: Mean value of the total invariant W in the turbulent phase as a function of l_s/l_T. We can see the reduction of the mean value of W near the critical value for linear instability $l_s/l_T = 28$, which means there is a reduction of turbulent transport.

4.2. ITG turbulence with finite density gradient

In this section, the result of a run for $l_s/l_T = 30$, $l_s/l_n = 2$, $l_s/l_V = 0$ and $M = 0$ is presented. This numerical run was done in order to retrieve information on the effect of a finite density gradient on the pure ITG turbulence results of the last section. Figure 8 shows a comparison between the time traces of the total zonal component of the invariant for $l_s/l_n = 0$ and $l_s/l_n = 2$ for fixed $l_s/l_T = 30$. We see that with finite density gradient there is also a quench of the total invariant when the zonal flows grow.

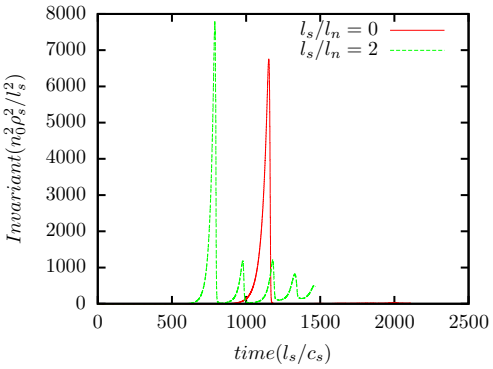

Figure 8: Comparison between runs with no density gradient and finite density gradient. The other parameters are kept fixed at $l_s/l_T = 30$, $l_s/l_V = 0$, $M = 0$.

4.3. Nonlinear results with finite M

In this section some results are presented for runs with finite external shear flow M. Here, the tem-

perature gradient is fixed at a value $l_s/l_T = 35$ in order to compare the results with the previous run, where $M = 0$, which coresponds to the run with $l_s/l_T = 35$ in figure 5. Runs were made for $M = 0.1$, $M = 0.2$, $M = 0.3$ and $M = 0.8$, with $l_s/l_V = 30M$ in order to fix the relation between the perpendicular and parallel components of the shear flow. The density gradient is set to $l_s/l_n = 0$ in all the runs.For the runs $M = 0.1$, $M = 0.2$ and $M = 0.3$ the same resolution parameters $nlx = nly = 64$ for the perpendicular plane are used with $L_x = L_y = 32\rho_s$. However, a higher parallel resolution $nlz = 1024$ with $L_z = 200\pi\cdot$ is used in order in order to obtain a better convergence of the results. For $M = 0.2$ and $M = 0.3$ there is no linear instability and therefore there is no turbulent transport. The mean values of the invariant in the turbulent phase are calculated and compared against the value of the previous run with $M = 0$ and $l_s/l_T = 35$ from figure 5. The results can be seen in figure 9.

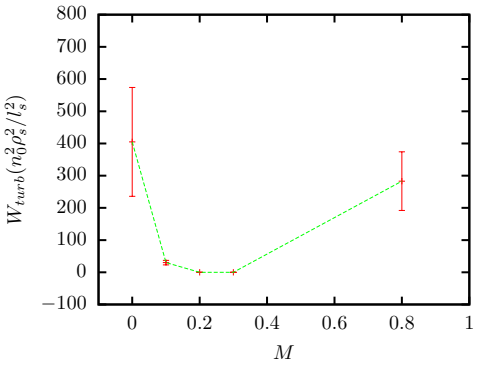

Figure 9: W_{turb} for different values of M at a fixed $l_s/l_T = 35$.

In this figure we see that the transport is first reduced due to the action of the external shear flow and is suppressed for $M = 0.2$. For $M = 0.8$ there is transport again, which should be due to the action of the PVG instability. More values are needed to clarify the analysis of these results.

5. Conclusions

In this work, theoretical and numerical (high-performance computing) studies were performed on the effect of background sheared flows in the nonlinear evolution of microinstabilities in magnetic confinement fusion plasmas. The first stage of the problem consisted in modifying the existent code *Viriato*, so that it could simulate the system of equations derived in [1]. In the second stage, the benchmark of the modified code was done against analytical results. In the third and final stage an analytical analysis of the system and nonlinear simulations were done .

5.1. Achievements

The modified code was obtained and it was benchmarked against the analytical solution obtained for the case $M = 0$, presented here in section 2.4 and derived in [1].

Analytical results were obtained in relation to an invariant of the system and the presence of zonal flows in the system. The zonal and non-zonal components of the invariants were obtained. It was shown that the system of equations composed by the the time evolution equations of the zonal and non-zonal components of the invariant derived for this system should behave as a predator-prey system, in which the predators are the zonal flows and the preys are the drift waves in the system. The linear instability of the zonal flows was worked out analytically.

The nonlinear simulations that we carried out revealed the presence of zonal flows in this system, and the consequent Dimit shift-like transport behavior. This is consistent with our expectation derived from the analytical analysis. The predator-prey nature of the system was observed, where the preys are the drift waves and the predators are the zonal flows. This means that simulations showed that the a significant growth of zonal flows can lead to a reduction of the transport due to drift waves. However, in some cases the transport can grow again, followed by a new growth of the zonal flows, which leads to a new reduction of transport. This cycle is observed until a steady state is achieved. It was seen that the introduction of a finite density gradient did not, significantly, change the results obtained for only finite temperature gradient.

It was also verified that an external shear flow can reduce turbulent transport and even suppress it completely. For a large value of external flow turbulence was observed due to PVG instability, but this is a preliminar result.

5.2. Future Work

The nonlinear results obtained should be tested with more resolution and bigger resolution domains. More nonlinear results should be obtained, in order to better map the values of the mean of the invariant in the turbulent phase for different combinations of the input parameters l_s/l_n, l_s/l_T, l_s/l_V and M, as it was done in [1] for the linear growth rate. Importantly, more results with external shear flow should be obtained to clarify the generation of turbulence by PVG instability and the saturation mechanism of this turbulence. Runs for large values of M should be done, in order to study, the existence of subcritical turbulence due to PVG instability. It would also be interesting to see if there is a Dimits shift-like behavior for the PVG instability.

Acknowledgements
I would like to thank my supervisors Prof. Nuno Loureiro and Doctor Luís Fazendeiro for the support. I would also like to thank the IFER-CSC support, as the computational time used in this work was provided by the supercomputer HELIOS

References

[1] S. L. Newton, S. C. Cowley and N. F. Loureiro. Understanding the effect of sheared flow on microinstabilities. *Plasma Physics and Controlled Fusion*, 52, 2010. doi: 10.1088/0741-3335/52/12/125001.

[2] J. Freidberg. *Plasma Physics and Fusion Energy*. Cambridge University Press, 1^{st} edition, 2007.

[3] E. J. Doyle, W. A. Houlberg, Y. Kamada *et al.* ITER Physics Basics Chapter 2: Plasma Confinement and Transport. *Nuclear Fusion*, 47:18–127, 2007. doi: 10.1088/0029-5515/39/12/302.

[4] Y.-c. Ghim, A. Field, A.A. Schekochihin *et al.* Local dependence of ion temperature gradient on magnetic configuration, rotational shear and turbulent heat flux in MAST. *Nuclear Fusion*, 54(4), 2014. doi: 10.1088/0029-5515/54/4/042003.

[5] C. M. Roach, I. G. Abel, R J Akers *et al.* Gyrokinetic simulations of spherical tokamaks. *Plasma Physics and Controlled Fusion*, 51, 2009. doi: 10.1088/0741-3335/51/12/124020.

[6] M. Barnes, F. I. Parra, E. G. Highcock *et al.* Turbulent transport in tokamak plasmas with rotational shear. *Physical Review Letters*, 106(17), 2011. doi: 10.1103/PhysRevLett.106.175004.

[7] P. H. Diamond and Y. -B. Kim. Theory of mean poloidal flow generation by turbulence. *Physics of Fluids B*, 3:1626–1633, 1991. doi: 10.1063/1.859681.

[8] P. H. Diamond, S.-I. Itoh, K. Itoh and T. S. Hahm. Zonal flows in plasma-a review. *Plasma Physics and Controlled Fusion*, 47(5), 2005. doi:10.1088/0741-3335/47/5/R01.

[9] K. Itoh, S.-I. Itoh, P. H. Diamond *et al.* Physics of zonal flows. *Physics of Plasmas*, 13, 2006. doi: 10.1063/1.2178779.

[10] F. F. Chen. *Introduction to Plasma Physics*. Cambridge University Press, Plenum, New York edition, 1974.

[11] G. G. Howes, S. C. Cowley, W. Dorland *et al.* Astrophysical Gyrokinetics: Basic Equations and Linear Theory. *The Astrophysical Journal*, 651(1):590–614, 2006. doi: 10.1086/506172.

[12] G. G. Howes, S. C. Cowley and J. C. McWilliams. Local Buoyant Instability of Magnetized Shear Flows. *The Astrophysical Journal*, 560(2), 2001. doi: 10.1086/322956.

[13] M. Landreman, T. M Antonsen Jr. and W. Dorland. Universal Instability for Wavelengths below the Ion Larmor Scale. *Physical Reviews Letters*, 114, 2015. doi: 10.1103/PhysRevLett.114.095003.

[14] S. C. Cowley, R. M. Kulsrud and R. Sudan. Considerations of ion temperature gradient driven turbulence. *Physics of Fluids B*, 3, 1991. doi: 10.1063/1.859913.

[15] P. J. Catto, M. N. Rosenbluth and C. S. Liu. Parallel velocity shear instabilities in an inhomogeneous plasma with a sheared magnetic field. *Physics of Fluids*, 16, 1973. doi: 10.1063/1.1694200.

[16] R. Numata, R. Ball and R. L. Dewar. Bifurcation in electrostatic resistive drift wave turbulence. *Physics of Plasmas*, 85(25), 2000. doi: 10.1103/PhysRevLett.85.5336.

[17] A. M. Dimits, G. Bateman, M. A. Beer *et al.* Comparisons and physics basis of tokamak transport models and turbulence simulations. *Physics of Plasmas*, 7, 2000. doi: 10.1063/1.873896.

[18] N. F. Loureiro, W. Dorland, L.Fazendeiro *et al.* Viriato: A FourierHermite spectral code for strongly magnetized fluidkinetic plasma dynamics. *Computer Physics Communications*, 206:45–63, 2016. 10.1016/j.cpc.2016.05.004.

[19] N. F. Loureiro and G. W. Hammett. An iterative semi-implicit scheme with robust damping. *Journal of Computational Physics*, 227:4518–4542, 2008. doi: 10.1016/j.cpc.2016.05.004.

[20] C. Hirsch. *Numerical Computation of Internal and External Flows, Volume 1: Fundamentals of Numerical Discretization*. John Wiley & Sons, 1988.

[21] W. H. Press, S. A. Teukolsky, W. T. Vetterling *et al. Numerical Recipes in C: The Art of Scientific Computing*. Cambridge University Press, 1997.